Nano Research
2024, 17(6): 5011–5021

ISSN 1998-0124 CN 11-5974/O4
https://doi.org/10.1007/s12274-024-6513-9

Research Article

# Asymmetrically coordinated main group atomic In-$S_1N_3$ interface sites for promoting electrochemical $CO_2$ reduction

Yan Gao[1] (✉), Jinlong Ge[1], Jingqiao Zhang[2,3], Ting Cao[2,3], Zhiyi Sun[5], Wensheng Yan[6], Yu Wang[7], Jie Lin[4] (✉), Wenxing Chen[5], and Zheng Liu[2,3] (✉)

[1] *Anhui Provincial Engineering Laboratory of Silicon-based Materials, Bengbu University, Bengbu 233030, China*
[2] *State Key Laboratory of Environmental Criteria and Risk Assessment, Chinese Research Academy of Environmental Sciences, Beijing 100012, China*
[3] *SEPA Key Laboratory of Eco-Industry, Chinese Research Academy of Environmental Sciences, Beijing 100012, China*
[4] *Ningbo Institute of Materials Technology and Engineering, Chinese Academy of Science, Ningbo 315201, China*
[5] *Energy & Catalysis Center, School of Materials Science and Engineering, Beijing Institute of Technology, Beijing 100081, China*
[6] *National Synchrotron Radiation Laboratory, University of Science and Technology of China, Hefei 230029, China*
[7] *Shanghai Synchrotron Radiation Facilities, Shanghai Institute of Applied Physics, Chinese Academy of Science, Shanghai 201204, China*



**Received:** 29 November 2023 / **Revised:** 20 January 2024 / **Accepted:** 23 January 2024

## ABSTRACT

Designing catalysts with highly active, selectivity, and stability for electrocatalytic $CO_2$ to formate is currently a severe challenge. Herein, we developed an electronic structure engineering on carbon nano frameworks embedded with nitrogen and sulfur asymmetrically dual-coordinated indium active sites toward the efficient electrocatalytic $CO_2$ reduction reaction. As expected, atomically dispersed In-based catalysts with In-$S_1N_3$ atomic interface with asymmetrically coordinated exhibited high efficiency for $CO_2$ reduction reaction ($CO_2$RR) to formate. It achieved a maximum Faradaic efficiency (FE) of 94.3% towards formate generation at −0.8 V vs. reversible hydrogen electrode (RHE), outperforming that of catalysts with In-$S_2N_2$ and In-$N_4$ atomic interface. And at a potential of −1.10 V vs. RHE, In-$S_1N_3$ achieves an impressive Faradaic efficiency of 93.7% in flow cell. The catalytic performance of In-$S_1N_3$ sites was confirmed to be enhanced through *in-situ* X-ray absorption near-edge structure (XANES) measurements under electrochemical conditions. Our discovery provides the guidance for performance regulation of main group metal catalysts toward $CO_2$RR at atomic scale.

## KEYWORDS

indium single-site catalyst, main group metal, asymmetrical coordination, $CO_2$ reduction reaction, structure–activity relationship

## 1 Introduction

Using green electricity to reduce $CO_2$ to value-added products is an effective way to alleviate the energy crisis and environmental problems, allowing sustainable use of carbon [1–8]. However, the electrochemical $CO_2$ reduction reaction ($CO_2$RR) involves multiple proton and electron transfer processes, which lead to its sluggish kinetics [9–13]. Moreover, it's challenging to activate the thermodynamically stable C=O bonds due to the chemical inertness of fully oxidized $CO_2$ [14–19]. Therefore, the potential required to drive $CO_2$RR is large, resulting in additional energy consumption. Unfortunately, the similar thermodynamic redox potentials of different $CO_2$RR products such as CO, formate, and methane bring about the poor reactivity and selectivity for the target products [20–22]. Consequently, it's of vital importance to develop high-efficiency $CO_2$RR electrocatalysts with low overpotentials for eliminating the large thermodynamic energy barriers, speeding up the kinetics, and achieving good selectivity to the target product.

As a liquid fuel with high energy density, formate is considered a desirable alternative for liquid hydrogen storage or release, which made it an attractive $CO_2$ emission reduction product [5, 23–25]. Noble metal catalysts attracted widely attention due to their excellent $CO_2$RR performance [26–28]. Whereas, the scarcity and high-cost restrict their growth potential [29, 30]. Furthermore, transition metal catalysts such as Co, Fe, Cu, and Mn are reported to perform high activity for $CO_2$RR, but low selectivity to formate [31–34]. Recently, main group metals (such as In, Sn, Sb, and Bi) have received extensive attention due to their excellent selectivity for formate from $CO_2$RR [35–39]. Recent studies have shown that oxide- or sulfide-derived metals can largely reduce the overpotentials of $CO_2$RR relative to pristine metals [40, 41]. For example, Zhang et al. were also able to obtain Bi-$N_4$ structures by pyrolysis of Bi-based metal-organic frameworks (MOFs), obtaining 97% CO Faradaic efficiency (FE) at lower overpotentials [42]. The study demonstrated that the oxidation state of surface In can enhance the adsorption affinity of $CO_2$ on the catalyst surface. Furthermore, the incorporation of an optimal amount of sulfur was found to facilitate the activation of $CO_2$, thereby enhancing the activity of $CO_2$RR. However, the nanostructures consist of metal and other active components, making the identification of active sites and how they affect $CO_2$RR remain elusive [5, 43–46]. Up to now, the main group metal–N–C single atom catalysts have

Address correspondence to Yan Gao, gaoyan@bbc.edu.cn; Zheng Liu, liuzheng@craes.org.cn; Jie Lin, linjie@nimte.ac.cn

recently emerged as efficient $CO_2RR$ catalysts [47–50]. Especially the single atom catalysts with M–$N_4$ (M = Sb, In, Sn, Bi, etc.) atomic interface exhibited the superior activity [51–53]. Furthermore, it's reported that the above catalysts can be modified by the formation of novel coordination configuration via importing extra metals or heteroatoms. Whereas, precisely tuning the coordination structure of porphyrin-like main group M–$N_4$ sites for efficient $CO_2RR$ has rarely been investigated.

To balance the catalytic activity and formate selectivity for $CO_2RR$ and enhance the understanding of reaction active sites in the molecular level, asymmetrically coordinated In single atom catalysts with different S and N coordination numbers (In-$S_1N_3$) were constructed by atomic interface engineering. Outstandingly, the engineered In-$S_1N_3$ demonstrated a maximum formate Faradaic efficiency ($FE_{HCOO^-}$) of 94.3% at −0.8 V vs. reversible hydrogen electrode (RHE), exceeding the In-$S_2N_2$ and In-$N_4$ catalysts. Since the activity and durability of single atom catalysts depend highly on the local coordination configuration, our findings highlight the significance of coordination regulating toward reactive sites in triggering high efficiency $CO_2RR$.

## 2 Experimental

### 2.1 Materials and chemicals

Indium chloride ($InCl_3$), dicyandiamide (DCDA), trimesic acid, sulfur powder, sodium sulfide ($Na_2S{\cdot}9H_2O$), ethanol, and Nafion D-521 dispersion (5% w/w in water and 1-propanol) were purchased from Alfa Aesar. Methanol and $KHCO_3$ were obtained from Sinopharm Chemical. Sulphuric acid ($H_2SO_4$, 98%) was obtained from Beijing Chemical Reagents. The deionized (DI) water used in all experiments was obtained through ion-exchange and filtration. All the chemicals were analytical grade and used without further purification.

### 2.2 Preparation of S precursor

In a typical synthesis, $Na_2S{\cdot}9H_2O$ (140.4 mg) was dissolved in DI water (11.7 mL) and subsequently S powder (32 mg) was added in the above solution while ultrasonic dissolving. After ultrasonic dissolving for 5 h at room temperature, the yellow clear and transparent solution was heated at 80 °C for 12 h in a Teflon autoclave. The S precursor was obtained after the solution was cooled down to room temperature.

### 2.3 Preparation of In-$S_xN_y$

In-$S_xN_y$ samples were prepared by a pyrolysis strategy. Different In-$S_xN_y$ samples were synthesized by changing the metal coordination by adjusting the amount of S source added. 50 mg of $InCl_3$, 1.2 g of DCDA, and 0.12 g of trimesic acid were dissolved in 5 mL of deionized water. The S precursor (2 mL) was added to the mixed solution with vigorous stirring. The solution was continuously stirred for 2 h and then dried at 80 °C. The obtained dry mixture was placed in a porcelain boat. The porcelain boats were placed in a tube furnace and annealed at a heating rate of 5 °C·min$^{-1}$ to 900 °C for 2 h under $N_2$ atmosphere, followed by natural cooling to room temperature. The samples were leached in 0.5 M $H_2SO_4$ solution at 80 °C for 24 h to remove the free metal residue, followed by thorough washing with ethanol and deionized water. Finally, In-$S_1N_3$ was obtained by vacuum drying at 60 °C overnight. In-$N_4$ was prepared without the addition of S precursor during the preparation. The content of S precursor was adjusted to 4 mL to obtain In-$S_2N_2$.

### 2.4 Characterization

The morphology of the samples was characterized by transmission electron microscopy (TEM, FEI Tecnai G2 F20 S-Twin, an accelerating voltage of 200 kV) and field-emission scanning electron microscopy (FE-SEM, JEORJSM-6700F). The high-angle annular dark field scanning transmission electron microscopy (HAADF-STEM) images were obtained by JEOL JEM-ARM200F at an accelerating voltage of 200 kV. The crystal phases present in each sample were identified using powder X-ray diffraction (PXRD) patterns and were recorded on a Bruker D8 Advance powder X-ray diffractometer at a scanning rate of 5 °·min$^{-1}$, using Cu-K$\alpha$ radiation ($\lambda$ = 1.5406 Å). The X-ray photoelectron spectroscopy (XPS) measurements were performed with a PerkinElmer Physics PHI 5300 spectrometer using Al K$\alpha$ nonmonochromatic radiation. The Raman measurements were taken on a Renishaw spectrometer at 532 nm on a Renishaw Microscope System RM2000. The $N_2$ adsorption/desorption curve was performed at 77 K using a Micromeritics ASAP 2020 surface area analyzer.

### 2.5 Electrochemical measurements

The electrochemical measurements were performed with a CHI760E electrochemical workstation using a gas-tight H-type cell in 50 mL 0.5 M $KHCO_3$ electrolyte at room temperature. Nafion 117 membrane was inserted between the cathodic chamber and anodic chamber. In-$S_1N_3$ and other control samples, the graphite rod, and Ag/AgCl (saturated KCl) electrode were employed as the working, counter, and reference electrodes, respectively. The electrolyte was 0.5 M $KHCO_3$. Before all measurements, $CO_2$ flow was used through the electrolyte in the cell for 30 min to obtain $CO_2$-saturated electrolyte. The cyclic voltammetry (CV) experiments were cycled in $CO_2$-saturated 0.5 M $KHCO_3$ with a scan rate of 50 mV·s$^{-1}$, and the linear sweep voltammetry (LSV) experiments were cycled in $CO_2$-saturated 0.5 M $KHCO_3$ with a scan rate of 10 mV·s$^{-1}$. All the potentials were calculated to the RHE by the equation $E_{RHE} = E_{Ag/AgCl} + 0.0591 \times pH + 0.197$ V. Chronopotentiometry was used to evaluate the stability of electrode materials. For comparison, In-$N_4$ and In-$S_2N_2$ were also loaded on a bare glassy carbon (GC) in the form of catalyst ink, which contained a certain content of catalyst, ethanol, and 5 wt.% Nafion solution. All the potentials were reported versus the RHE.

In addition, the catalysts were performed at ambient environment on the electrochemical workstation (SP-150, Bio-Logic) in a flow cell configuration. The catalyst-modified carbon paper electrode was the working electrode. Platinum tablets and Ag/AgCl electrodes were used as the counter and reference electrodes, respectively. The cathode compartment and anode compartment were separated by an anion exchange membrane. And the electrolyte was 1 M KOH (pH = 14). During the electrocatalytic $CO_2RR$ experiments, the polarization curves were performed by LSV mode at a scan rate of 8 mV·s$^{-1}$ in 1 M KOH solution with $CO_2$/Ar flowing. All the LSV curves and electric reduction $CO_2$ were carried out with 90% *iR* compensation. All the potentials were measured versus Ag/AgCl electrode, and the results were reported versus RHE based on the Nernst equation: $E$ (vs. RHE) = $E$ (vs. Ag/AgCl) + 0.1989 V + 0.0596 × pH. Solution resistance ($R_u$) was determined by potentiostatic electrochemical impedance spectroscopy at a sinusoidal potential frequency of 100 kHz with 20 mV amplitude centered on the electrolysis potential just before electrolysis.

### 2.6 Theoretical calculation

The Vienna *ab initio* simulation package (VASP) was applied to perform all the density functional theory (DFT) calculations, and the electron ion interaction was described with the projector augmented wave (PAW) method. The electron exchange and

correlation energy were solved with the revised Perdew–Burke–Ernzerhof (RPBE) exchange-correlation functional within the generalized gradient approximation. An energy cut-off of 500 eV and a second-order Methfessel–Paxton electron smearing with $\sigma$ = 0.2 eV were used to guarantee the accuracy. The convergences criteria for energy and force were set to be 10–5 eV and 0.02 eV·Å$^{-1}$, respectively. To avoid obvious interactions, a vacuum layer of 15 Å was set between the periodically repeating slabs. Spin polarization was included throughout all the simulations. The In-$S_1N_3$ catalyst was modeled by a $p(4 \times 4)$ supercell of graphene doped with nitrogen. As comparisons, a $p(4 \times 4)$ supercell was applied to simulate the In-$S_2N_2$ and In-$N_4$ catalyst. ($3 \times 3 \times 1$) Monkhorst–Pack grid $K$-points was used to sample the Brillouin zone for all three models. The free energies of the reaction was calculated with computational hydrogen electrode (CHE) model as developed by Norskov's group, which provides an elegant approach of avoiding the explicit treatment of solvated protons. Note that the difference between limiting potentials for $CO_2$ reduction and $H_2$ evolution ((i.e., $\Delta U = U_L(CO_2) - U_L(H_2)$, where $U_L = -\Delta G_{0/e}$) had been widely applied to describe the selectivity of the $CO_2$ER, and a more positive $\Delta U$ value denoted a higher selectivity.

## 3 Results and discussion

### 3.1 Synthesis of In-$S_1N_3$ and reference samples

As illustrated in Fig. 1(a), the In-$S_1N_3$ catalysts were firstly fabricated via a wet-impregnation process, then followed by pyrolysis process. Experimentally, DCDA and trimesic acid as the source of nitrogen and carbon were thoroughly mixed with $InCl_3$ and sulfur powder in alcoholic solution. Subsequently, the obtained dry powder is calcined at $N_2$ atmosphere and acid etching into N and S asymmetrically dual-coordinated In active sites embedded in carbon matrix. Furthermore, the S and N coordination numbers were attempted to control through regulating the amount of S-derived precursors added during annealing. Consequently, the In-$S_1N_3$ and In-$S_2N_2$ were obtained

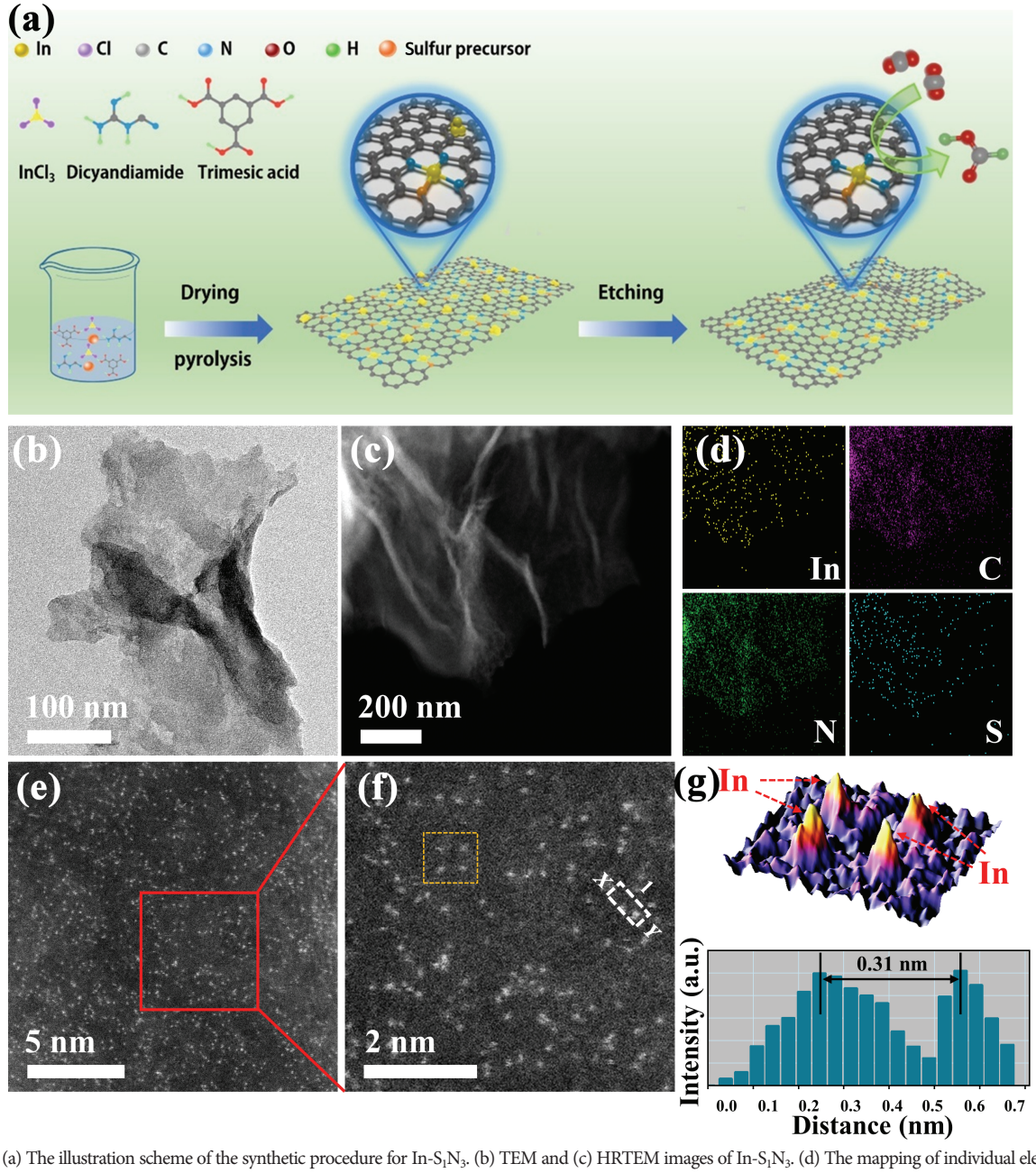


**Figure 1** (a) The illustration scheme of the synthetic procedure for In-$S_1N_3$. (b) TEM and (c) HRTEM images of In-$S_1N_3$. (d) The mapping of individual elements (In, C, N, and S) of In-$S_1N_3$. (e) HAADF-STEM image of In-$S_1N_3$. (f) The magnified HAADF-STEM image of In-$S_1N_3$. (g) 3D model of isolated In atom bright spots along the yellow dotted line and the corresponding intensity profiles along the line $X$–$Y$ in (f).

at 900 and 1000 °C, respectively. As the comparison, N-coordinated In active sites embedded in carbon matrix (In-$N_4$) was prepared without the addition of sulfur powder.

To visually examine the morphology of the synthesized samples, we conducted TEM and energy-dispersive X-ray spectroscopy (EDS) measurements. TEM image analysis indicates that In-$S_1N_3$ exhibits a nanosheet structure resembling graphene, with no detectable small particles of In species on the surface (Fig. 1(b)). This consistent with the PXRD results in Fig. S1 in the Electronic Supplementary Material (ESM) that In-$S_1N_3$ shows the merely diffraction peaks corresponding to graphitic carbon, and no characteristic peak assigned to In crystals was observed. Raman spectra suggest that the carbon substrates of In-$S_1N_3$, In-$S_2N_2$, and In-$N_4$ all are disordered with a large number of defects (Fig. S2 in the ESM). The high surface area of In-$S_xN_y$ was confirmed through $N_2$ absorption–desorption isotherms (Fig. S3 in the ESM), which revealed a higher specific surface area compared to other samples. The EDS images of In-$S_1N_3$ (Figs. 1(c) and 1(d)) demonstrate that the element In, S, and N were uniformly distributed on the surface of the graphene-like carbon nanosheets. Furthermore, the HAADF-STEM images was utilized to directly monitor the monodispersing of In due to its sub-angstrom resolution. The isolated In atoms of In-$S_1N_3$ were identified with the atomically dispersed bright dots in Figs. 1(e) and 1(f), which were further confirmed by the three-dimensional (3D) atomic energy intensity diagram along the yellow dotted line and the intensity profiles and *X*–*Y* in Fig. 1(g). That is, the distance between two In atoms in In-$S_1N_3$ (at least 0.31 nm) exceeds the In-effective atomic diameter. According to the inductively coupled plasma optical emission spectrometry (ICP-OES) analysis, the In species content in In-$S_1N_3$ was 4.5 wt.%. In addition, the S,N-co-doped carbon (SNC), In-$N_4$, and In-$S_2N_2$ samples were also

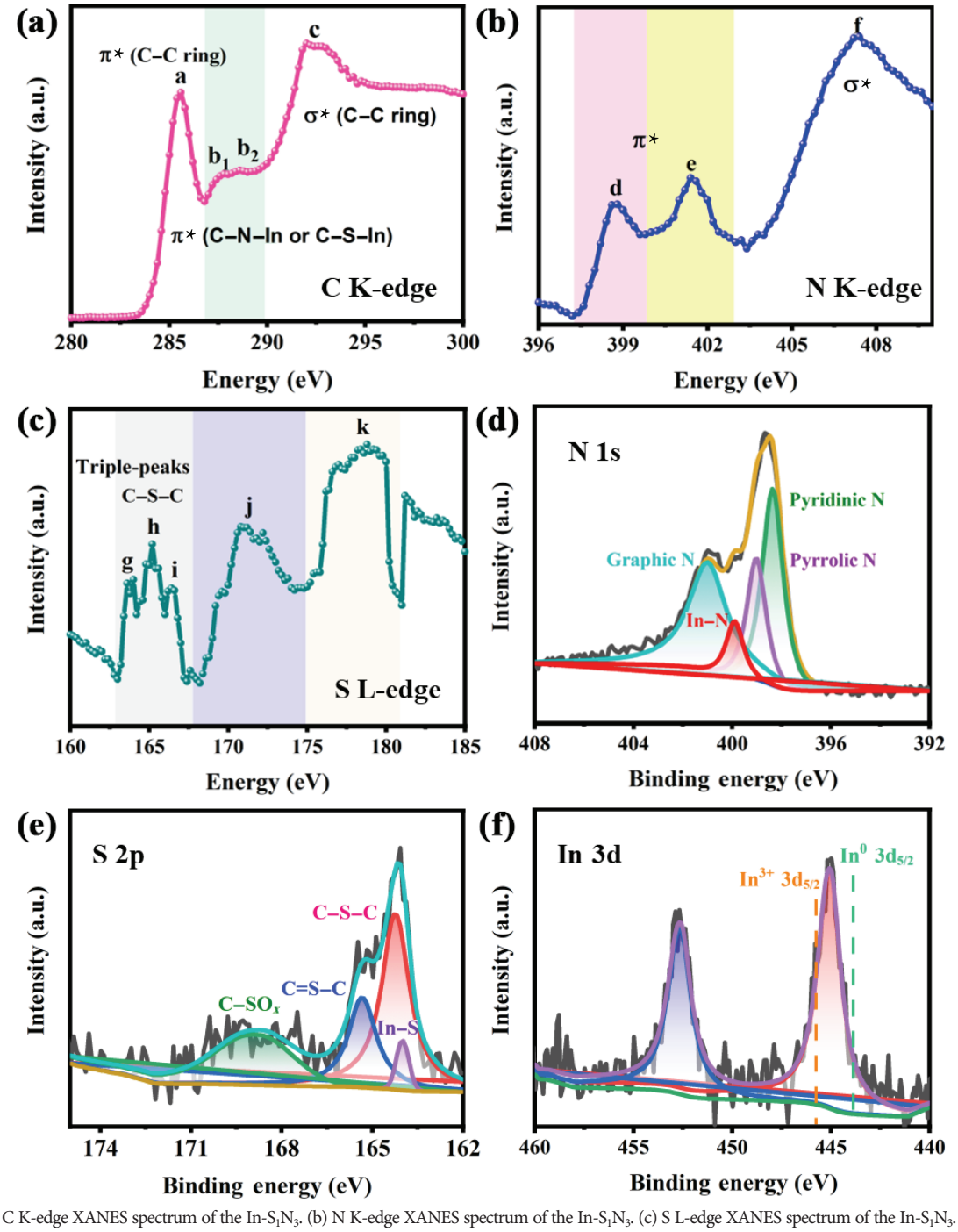


**Figure 2** (a) C K-edge XANES spectrum of the In-$S_1N_3$. (b) N K-edge XANES spectrum of the In-$S_1N_3$. (c) S L-edge XANES spectrum of the In-$S_1N_3$. (d) N 1s, (e) S 2p, and (f) In 3d XPS spectra of In-$S_1N_3$.

characterized for comparison. As elucidated in Figs. S4 and S5 in the ESM, all the reference samples performed the same graphene-like structure. Moreover, the isolated feature of In atoms in In-$N_4$ and In-$S_2N_2$ was also verified by the same characterization instruments as In-$S_1N_3$.

### 3.2 Characterization of coordination structure

To examine the electronic structure and the interatomic interaction of In, S, N, and C in In-$S_1N_3$, synchrotron-radiation-based soft XANES and XPS measurements were performed. For the C K-edge spectrum (Fig. 2(a)), four distinct peaks situated at 285.6 (peak a), 287.7 (peak $b_1$), 288.6 (peak $b_2$), and 292.3 eV (peak c) are obviously observed [54]. These peaks correspond to the dipole transition of the C 1s core electron into π* C=C, π* C–N/S–C, and σ* C–C antibonding orbitals, indicating the formation of In–N/S bonds at the atomic interface of In-$S_1N_3$. As depicted by the N K-edge spectrum in Fig. 2(b), three characteristic peaks at 398.7 (peak d), 401.4 (peak e), and 407.3 eV (peak f) could be assigned to the pyridinic N, pyrrolic N, and graphitic N, respectively [55]. Moreover, S L-edge spectrum of In-$S_1N_3$ was dominated by the peaks located in the region of 163–167 eV, which could be attributed to C–S–C coordination species and suggested the formation of S in the carbon matrix [56, 57] (Fig. 2(c)). In addition, the electronic structure was further investigated by XPS analysis. Obviously, the N 1s XPS spectra in Fig. 2(d) possessed four peaks at binding energies of 398.4, 399.1, 399.9, and 401.0 eV for pyridinic N, pyrrolic N, In-N, and graphitic N, respectively, indicating the formation of In–N bond in the entire architecture. As shown in Fig. 2(e), the S 2p XPS spectra show four types of S species. The peaks at 165.3 and 164.2 eV are assigned to C=S–C and C–S–C bond, respectively. While the peak at 168.9 eV was associated to the sulfate species (C-$SO_x$). Notably, the characteristic peaks observed at 164.0 eV are attributed to the In–S bond, indicating the partial replacement of N atoms with S atoms around the In atoms. The In 3d spectra in Fig. 2(f) displayed the existence of In $3d_{3/2}$ and In $3d_{5/2}$ at 452.7 and 445.1 eV, respectively. while the peaks at 445.1 eV for In $3d_{5/2}$ situate between $In^0$ (443.8 eV) and $In^{3+}$ (445.7 eV), indicating the ionic $In^{\delta+}$ ($0 < \delta < 3$) nature of In in In-$S_1N_3$. All these results demonstrated that the atomically dispersed In in In-$S_1N_3$ manifested typical In-N and In-S asymmetrically dual-coordinating environment.

Synchrotron radiation-based hard X-ray absorption fine structure (XAFS) analysis was conducted to gain insight into the atomic-scale interface structure of In-$S_1N_3$ [58–60]. The In K-edge absorption threshold can determine the average oxidation state of In species. In the XANES curves (Fig. 3(a)), the positions of In-$S_1N_3$, In-$N_4$, and In-$S_2N_2$ are between In foil and $In_2O_3$, indicating that the average oxidation state of In is between 0 and +3. Figure 3(b) is the oxidation state of In catalyst obtained by the first-derivative XANES curves (Fig. S6 in the ESM). The fitted oxidation state of In in In-$S_1N_3$, determined from K-edge XANES spectra, was found to be 0.79, which is consistent with the results of XPS and XAFS results. In addition, the oxidation states of In-$S_2N_2$ and In-$N_4$ are 2.54 and 1.50, respectively, indicating that the

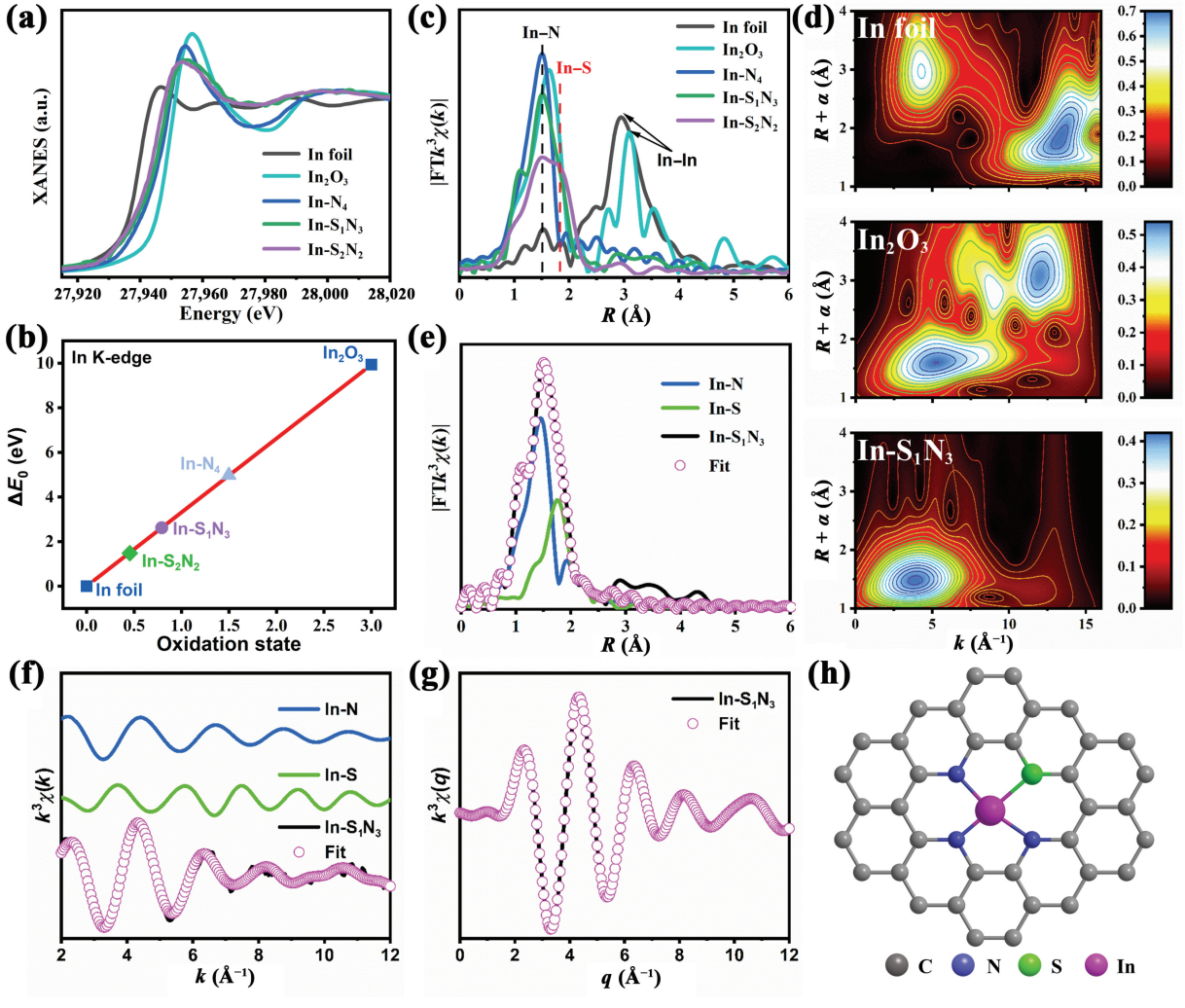


**Figure 3** (a) The In K-edge XANES and (b) FT-EXAFS spectra of In-$S_1N_3$ and the references. (c) Oxidation state of In-$S_1N_3$ and the references. (d) WT-EXAFS plots of In-$S_1N_3$, In foil, and $In_2O_3$. FT-EXAFS fitting curve of In-$S_1N_3$ in (e) *R* space, (f) *k* space, and (g) *q* space. (h) Atomic structure model of In-$S_1N_3$.

interface regulation of sulfur improves the local charge environment of the central In atom. The Fourier transform extended X-ray absorption fine structure (FT-EXAFS) spectra of In-$S_1N_3$ and the references (In-$N_4$, In-$S_2N_2$, In foil, and $In_2O_3$) are illustrated in Fig. 3(c). The results show that the distinct FT peak at 1.5 Å is ascribed to the In–N scattering. Comparing the FT-EXAFS spectra of In-$S_1N_3$ with In-$N_4$, In-$S_2N_2$, In foil and $In_2O_3$, it's noted that the emergence of the shoulder peak at 1.8 Å may be attributed to the In–S scattering, providing accurate evidence for the formation of In–S bonding (Table S1 in the ESM). Furthermore, the In–In scattering peaks are not seen for In-$S_1N_3$, In-$N_4$, and In-$S_2N_2$, compared with In foil. The wavelet transform (WT)-EXAFS technique is employed at the In K-edge to probe the atomic structure of In-$S_xN_y$, benefiting from its high resolution in both *k* and *R* spaces (Fig. 3(d) and Fig. S7 in the ESM). The WT contour plots of In-$S_1N_3$ exhibit a single intensity maximum at 4.2 $Å^{-1}$, which is attributed to the contributions of In–N and In–S pairs. In contrast, no In–In signals are detected, as observed in the WT plots of In foil. This further confirms the atomic dispersion of In atoms in In-$S_1N_3$.

Least-square EXAFS fitting of the In-$S_1N_3$ was performed to extract the structural parameters at In K-edge quantitatively, and the fitting results are exhibited in Figs. 3(e)–3(g). Notably, the experimental spectra match quite well with those of the fitting curves. Based on the EXAFS fitting results, it is concluded that the central atom In in $InS_1N_3$ was coordinated directly by one S atom and three N atoms. In other words, the atomically dispersed In was embedded in the carbon matrix in the form of unsymmetrical isolated In-$S_1N_3$ four-coordinated moieties. On the basis of the results for soft and hard XAFS, the local structure model for In-$S_1N_3$ is constructed in Fig. 3(h). In the EXAFS fitting results, the bond lengths of In–S and In–N are 2.39 and 1.97 Å, respectively. Moreover, the EXAFS analyses of In-$N_4$ and In-$S_2N_2$ are shown in Figs. S8 and S9 in the ESM for comparison.

### 3.3 Electrocatalytic $CO_2$ reduction performance test

The $CO_2$RR performance of In-$S_1N_3$ and the references were evaluated in $CO_2$-saturated 0.5 M $KHCO_3$ solution using a custom-made three electrode set-up (Fig. S10 in the ESM). The LSV curves in Fig. 4(a) demonstrated that the In-$S_1N_3$ achieved the highest total current density compared to that of In-$N_4$ and In-$S_2N_2$, indicating the superior catalytic activity for In-$S_1N_3$. Interestingly, In-$S_1N_3$ manifested a current density of 24.49 $mA·cm^{-2}$ at the potential of −1.0 V (vs. RHE), which is 1.61-fold and 2.21-fold relative to In-$S_2N_2$ (15.21 $mA·cm^{-2}$) and In-

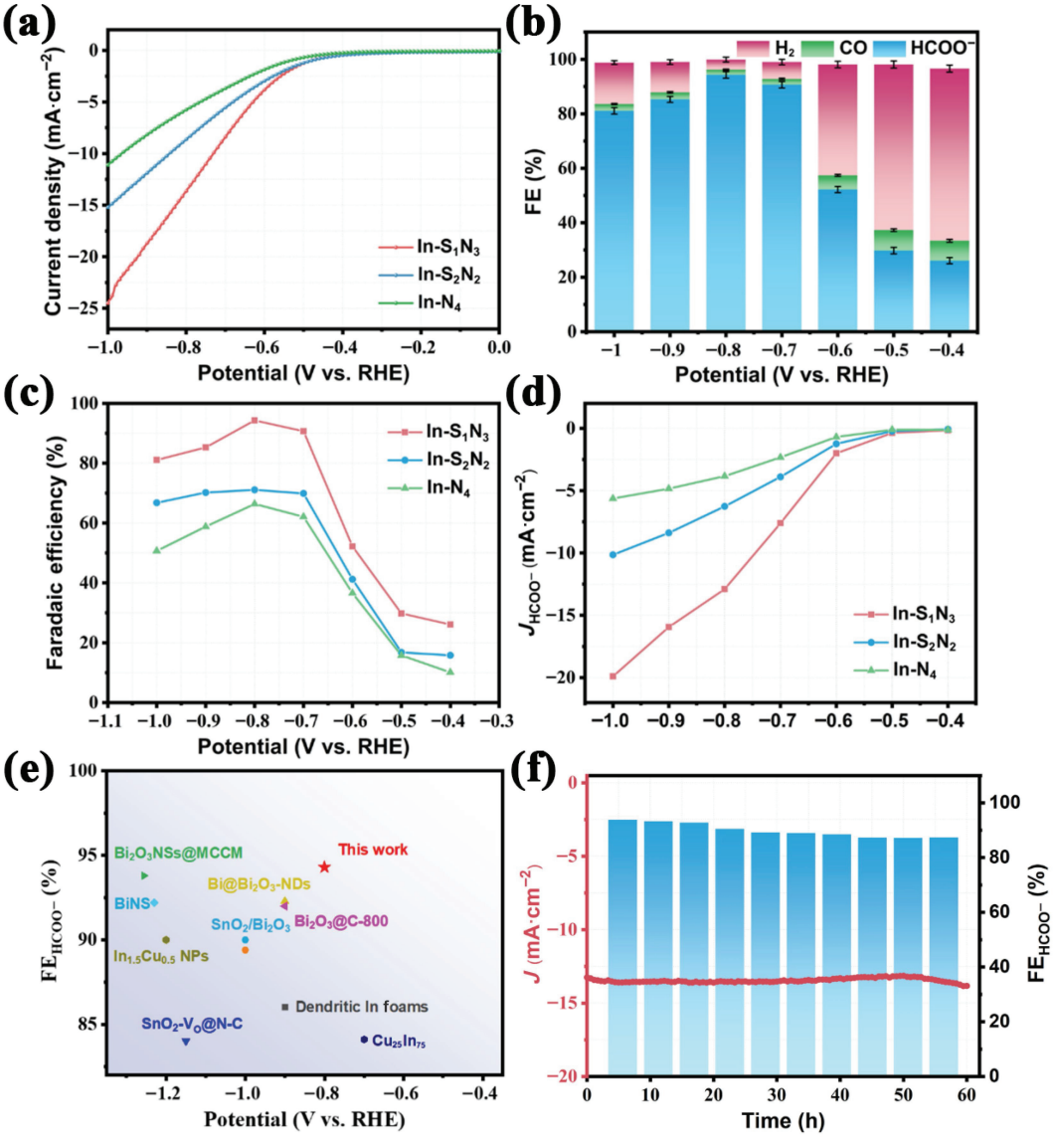


**Figure 4** (a) LSV curves of In-$S_1N_3$, In-$S_2N_2$, and In-$N_4$ performed in $CO_2$-saturated 0.5 M $KHCO_3$. (b) FEs of $H_2$, CO, and $HCOO^-$ at different potentials of In-$S_1N_3$ catalyst. (c) FEs for $HCOO^-$ of In-$S_1N_3$, In-$S_2N_2$, and In-$N_4$ at different potential. (d) $J_{HCOO^-}$ of In-$S_1N_3$, In-$S_2N_2$, and In-$N_4$. (e) The comparation of FEs for In-$S_1N_3$ with other reported catalysts. (f) Stability test of In-$S_1N_3$ at a potential of −0.80 V vs. RHE.

$N_4$ (11.09 mA·cm$^{-2}$), respectively. To probe the origin of the source of the current density, the LSV curve of the In-$S_1N_3$ in Ar-saturated $KHCO_3$ solution is conducted in Fig. S11 in the ESM. Compared with $CO_2$-saturated $KHCO_3$ solution, In-$S_1N_3$ exhibited lower current density in Ar-saturated $KHCO_3$ solution. The results indicated that the current density originated from the $CO_2$RR and In-$S_1N_3$ served as the active sites. Meanwhile, the poison experiments were carried out to further test the active species in $CO_2$RR. As displayed in Fig. S12 in the ESM, the current density of In-$S_1N_3$ presented explicit depression in the mixed solution of $KHCO_3$ and KSCN than the pure $KHCO_3$, confirming the In single atoms active sites for $CO_2$ER. Moreover, the FEs was carried out to identify the excellent selectivity of In-$S_1N_3$. The reaction products were detected periodically by gas chromatography (GC) and $^1$H nuclear magnetic resonance (NMR) spectroscopy (Fig. S13 in the ESM). It's noted that the gaseous and liquid products were $H_2$, CO, and formate and In-$S_1N_3$ attained the formate FEs of above 85% at −0.9 to −0.7 V vs. RHE (Fig. 4(b) and Fig. S14 in the ESM). The calculated formate FEs of In-$S_1N_3$, In-$N_4$, and In-$S_2N_2$ are shown in Fig. 4(c). Significantly, In-$S_1N_3$ reached a maximum $FE_{HCOO^-}$ of 94.3% at −0.8 V vs. RHE, which was higher than that of In-$S_2N_2$ (73.2% at −0.8 V) and In-$N_4$ (67.2% at −0.8 V), demonstrating the superior selectivity of In-$S_1N_3$ for formate.

In addition, the partial formate current density ($J_{HCOO^-}$) of In-$S_1N_3$, In-$N_4$, and In-$S_2N_2$ regarding the applied potentials is exhibited in Fig. 4(d). The value of $J_{HCOO^-}$ in In-$S_1N_3$ increased rapidly over the applied potentials, demonstrating the remarkable performances toward $CO_2$RR. Impressively, In-$S_1N_3$ obtained $J_{HCOO^-}$ of 12.90 mA·cm$^{-2}$ at −0.8 V, which is 2.04-fold and 3.33-fold higher than those of In-$S_2N_2$ (−6.32 mA·cm$^{-2}$) and In-$N_4$ (−3.87 mA·cm$^{-2}$), respectively. Besides, the $J_{HCOO^-}$ of In-$S_1N_3$ outperformed the other two samples at lower potentials. For example, $J_{HCOO^-}$ for In-$S_1N_3$ was −19.89 mA·cm$^{-2}$ at −1.0 V, exceeding those of In-$S_2N_2$ (−10.14 mA·cm$^{-2}$) and In-$N_4$ (−5.63 mA·cm$^{-2}$). Moreover, to bring insight into the reaction kinetics, Tafel slopes of different samples were performed and analyzed. The fitted Tafel slopes for In-$S_1N_3$, In-$S_2N_2$, and In-$N_4$ were 176.17, 226.07, and 293.55 mV·dec$^{-1}$, respectively (Fig. S15 in the ESM). This revealed that the kinetics was greatly enhanced with the In atom coordinated by one S atom and three N atoms. Additionally, Fig. 4(e) shows the comparable formate FEs for In-$S_1N_3$ with the state-of-the-art reported main group metal electrocatalysts (Table S2 in the ESM). Compared with other catalysts in the table, In-$S_1N_3$ has a higher current density. The long-term durability of In-$S_1N_3$ was tested at −0.80 V vs. RHE. Results indicated the negligible decay in the current density and $FE_{HCOO^-}$ after operation for 60 h (Fig. 4(f)). The EDS mapping images of In-$S_1N_3$ catalyst show that the In, S, and N species were uniformly dispersed on the carbon architecture after durability test, indicating the stability during the $CO_2$RR process (Fig. S16 in the ESM).

In order to investigate the industrial application of catalysts, we employed a flow cell based on gas diffusion electrodes (GDE) (Fig. S17 in the ESM). This method effectively overcomes the mass transfer limitations of $CO_2$, enabling $CO_2$ electrolysis to operate under conditions similar to industrial electrolyzers (Fig. 5(a)). Figure 5(b) depicts the LSV curves. These curves show that In-$S_1N_3$ demonstrates higher current density than In-$N_4$ and In-$S_2N_2$, indicating its superior catalytic activity. In Fig. 5(c), at a potential of −1.10 V vs. RHE, In-$S_1N_3$ achieves an impressive Faradaic efficiency of 93.7%. With the gradual increase of voltage from −1.1 to −1.4 V vs. RHE, the Faradaic efficiency of HCOOH will decrease to a certain extent. However, the HCOOH selectivity of In-$S_1N_3$ remains 86.2% when the voltage is increased to −1.4 V vs. RHE. Additionally, stability tests were conducted at high current for up to 20 h to assess the catalytic stability of IN-$S_1N_3$ (Fig. 5(d)). The findings indicate that the current remains stable at 200 mA·cm$^{-2}$ over 20 h, with formic acid selectivity exceeding 90%. The results demonstrate that the coordination of sulfur elements at the interface plays a crucial role in regulating the conversion of $CO_2$ to formic acid.

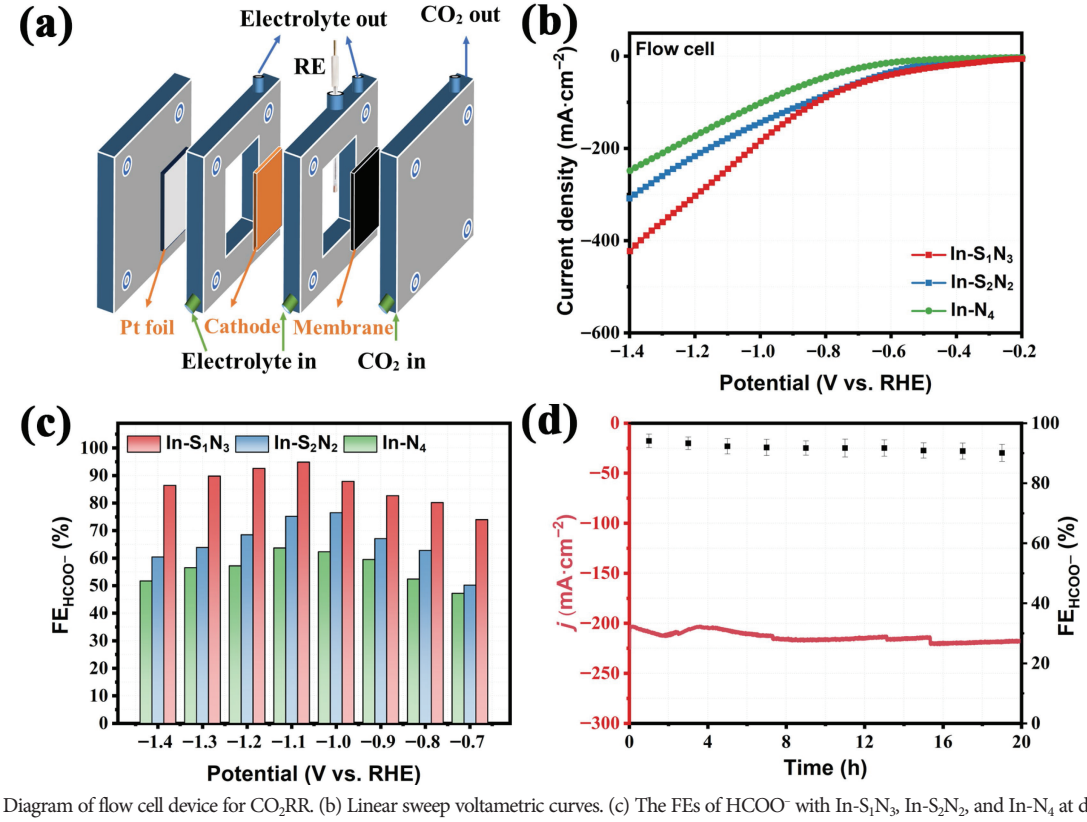


**Figure 5** (a) Diagram of flow cell device for $CO_2$RR. (b) Linear sweep voltametric curves. (c) The FEs of $HCOO^-$ with In-$S_1N_3$, In-$S_2N_2$, and In-$N_4$ at different applied potentials (−0.7 to −1.4 V vs. RHE). (d) Stability test of In-$S_1N_3$ at a potential of −1.10 V vs. RHE.

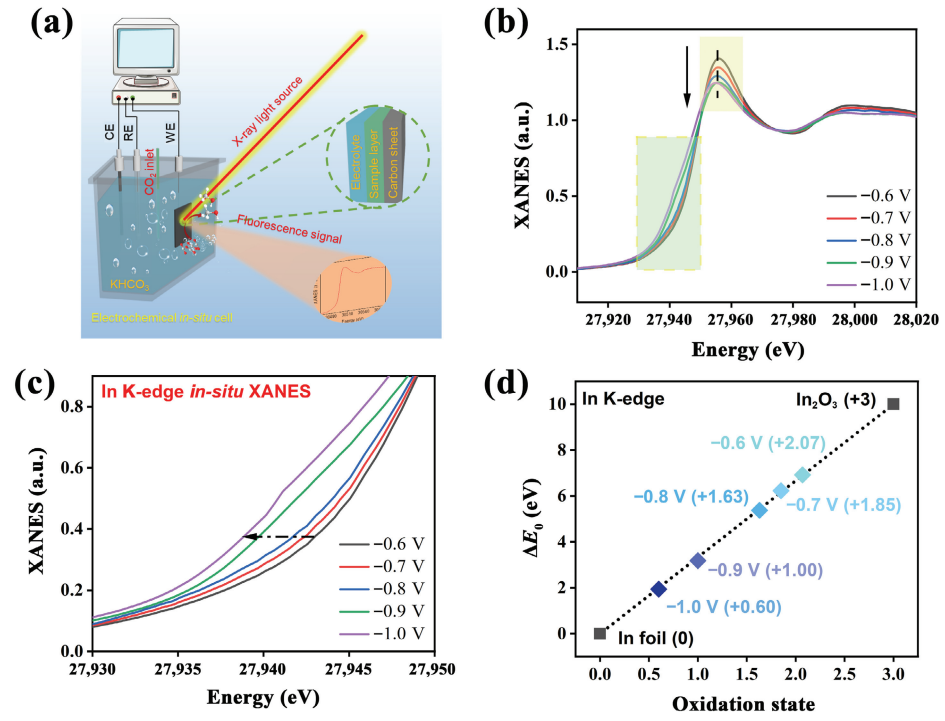


**Figure 6** (a) Diagram of homemade electrochemical cell device for *in-situ* XAFS. (b) In K-edge *in-situ* XANES and (c) the locally enlarged image of In-$S_1N_3$ from −0.6 to −1.0 V vs. RHE in 0.5 M $KHCO_3$. (d) Oxidation states of In species obtained from XANES spectra.

### 3.4 *In-situ* characterization

It is essential to investigate the atomic structure–activity relationship of the $CO_2$RR catalyst under *operando* conditions to elucidate the underlying reaction mechanism. In order to determine the actual catalytic sites of In-$S_1N_3$, *in-situ* XAFS spectra were utilized to directly observe its catalytic behavior. The *in-situ* XAFS tests were carried out using a home-made cell (Fig. 6(a)), and all the spectra were collected in fluorescence model by a common-used Lytle detector. As shown in Fig. 6(b), we found that when the potential is decreased from −0.6 to −1.0 V, the energy band edge of In K-edge shifted to lower energy binding, indicating that the oxidation state of In was lower during the reaction. The edge position amplification diagram of the XANES spectrum again proved that as the potential gradually increases, the In XANES edge shifted 0.5, 0.88, 1.90, and 1.96 V to the lower energy, respectively (Fig. 6(c)). Obviously, the oxidation state change of In atom indirectly proves that In-$S_1N_3$ is the active site of $CO_2$RR and the structure changes. The average oxidation states (Fig. 6(d)) indicate a decrease in the valence of In from 2.21 to 2.07, 1.85, 1.63, 1.00, and 0.60 for In-$S_1N_3$ at potentials ranging from *ex-situ* to −0.6, −0.7, −0.8, −0.9, and −1.0 V, respectively. *In-situ* EXAFS analysis was performed to monitor the evolution of the coordination configuration of single-atom In during $CO_2$RR. Figure S18 in the ESM displays the corresponding $k^3$-weighted FT-EXAFS spectra for In-$S_1N_3$ at −0.6, −0.7, −0.8, −0.9, and −1.0 V vs. RHE. At the corresponding applied potentials, the coordination of the In atoms with the N/S atoms does not change. The intensity of the In–N signal peak is almost constant as the voltage is gradually raised. The FT-EXAFS fitting results (Fig. S19 and Table S3 in the ESM) indicate the In-N/S coordination structure was almost unchanged at different reaction potentials. These results indicate that the lower oxidation state of In in In-$S_1N_3$ is more suitable for converting $CO_2$ into formic acid during $CO_2$RR.

### 3.5 DFT calculations

In order to better understand the impressive performance of In-$S_1N_3$ in formate production, we conducted DFT calculations to investigate the reaction mechanisms of $CO_2$ reduction on In-$S_1N_3$, In-$S_2N_2$, and In-$N_4$ (Fig. 7). Our simulations considered both formate and CO production pathways. The potential energy graphs (PES) of Figs. 7(a) and 7(b) show that the HCOO* formed by the initial proton–electron pair addition of all three catalysts is more energetically favorable than COOH*, indicating that the formic acid pathway plays a dominant role in $CO_2$ activation. Figure 7(a) shows that In-$S_1N_3$ (0.42 eV) has the lowest free energy to generate HCOO*, followed by In-$S_2N_2$ (0.68 eV) and In-$N_4$ (0.71 eV). This clearly highlights the different electrochemical performance trends of the three catalysts, namely In-$S_1N_3$ > In-$S_2N_2$ > In-$N_4$. In addition, Fig. 7(c) shows the PES of the hydrogen evolution reaction (HER), which is the main competing reaction of $CO_2$RR and has a great influence on the product. Importantly, the difference between the $CO_2$ reduction limit potential and the hydrogen evolution limit potential can be used to explain the selectivity advantage of $CO_2$RR, and the higher $\Delta U$ value indicates higher selectivity. Based on this, we compared the selectivity of the three catalysts, as shown in Fig. 7(d). The results show that In-$S_1N_3$ has the largest $\Delta U$ value, indicating excellent performance in the selective conversion of $CO_2$ to formate. The performance of In-$S_2N_2$ and In-$N_4$ is in line with the experimental results, demonstrating poor performance. These theoretical results explain the differences in $CO_2$RR activity and selectivity of different catalysts at the atomic level, and provide help to understand the atomic interface regulation and validate our experimental results.

## 4 Conclusions

In summary, the In single atom catalysts with asymmetric In-$S_1N_3$ atomic interface were constructed for energy conversion. The atomic configuration of In-$S_1N_3$ was determined by XANES and EXAFS analysis. As a result, the optimized electronic structures and atomic configuration of In-$S_1N_3$ bring about the remarkable activity and selectivity for $CO_2$RR. Finally, In-$S_1N_3$ exhibited superior $CO_2$RR performance to that of In-$S_2N_2$ and In-$N_4$. The catalytic performance of In-$S_1N_3$ site was improved by *in-situ* XANES under electrochemical conditions. This work not only

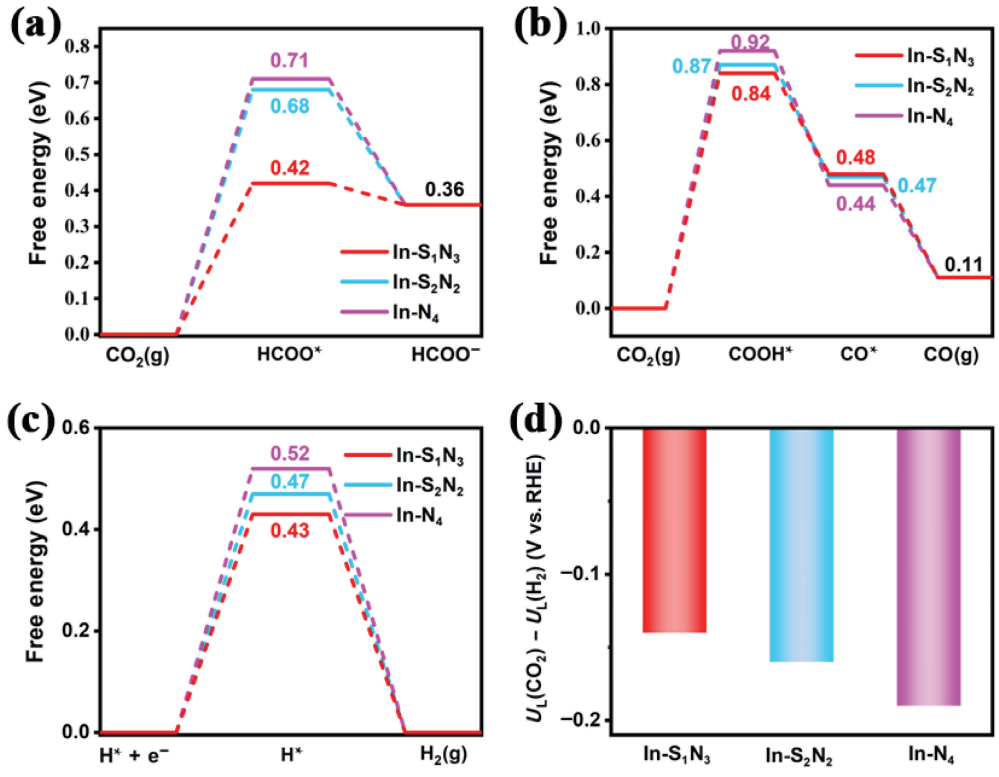


**Figure 7** Calculated potential free energy diagrams of $CO_2$ electroreduction to (a) formate, (b) CO, and (c) HER on In-$S_1N_3$, In-$S_2N_2$, and In-$N_4$ catalysts. (d) The limiting potentials for the total reaction on In-$S_1N_3$, In-$S_2N_2$, and In-$N_4$ catalysts.

presents a viable pathway for efficient $CO_2$RR but also offers a general and reliable approach for the synthesis of new atomically dispersed metal catalysts for energy conversion.

## Acknowledgements

This work was supported by the Anhui Provincial Department of Education (No. KJ2021A1125), the National Natural Science Foundation of China (No. 12374390), Ningbo 3315 Innovative Teams Program (No. 2019A-14-C), and the member of Youth Innovation Promotion Association Foundation of CAS, China (No. 2023310). The authors thank the BL14W1 in the Shanghai Synchrotron Radiation Facility (SSRF), BL10B and BL12B in the National Synchrotron Radiation Laboratory (NSRL) for help with characterizations.

**Electronic Supplementary Material:** Supplementary material (detailed experimental procedures; TEM, XRD, XPS, XAFS figures, etc.; and tables) is available in the online version of this article at https://doi.org/10.1007/s12274-024-6513-9.

## References

[1] Gao, D. F.; Arán-Ais, R. M.; Jeon, H. S.; Cuenya, B. R. Rational catalyst and electrolyte design for $CO_2$ electroreduction towards multicarbon products. *Nat. Catal.* **2019**, *2*, 198–210.

[2] Sun, Z. Y.; Hu, Y. N.; Zhou, D. N.; Sun, M. R.; Wang, S.; Chen, W. X. Factors influencing the performance of copper-bearing catalysts in the $CO_2$ reduction system. *ACS Energy Lett.* **2021**, *6*, 3992–4022.

[3] Xie, Y.; Ou, P. F.; Wang, X.; Xu, Z. Y.; Li, Y. C.; Wang, Z. Y.; Huang, J. E.; Wicks, J.; McCallum, C.; Wang, N. et al. High carbon utilization in $CO_2$ reduction to multi-carbon products in acidic media. *Nat. Catal.* **2022**, *5*, 564–570.

[4] Yang, X. F.; Wang, Q. R.; Chen, F. R.; Zang, H.; Liu, C. J.; Yu, N.; Geng, B. Y. *In-situ* electrochemical restructuring of $Cu_2BiS_x$ solid solution into Bi/$Cu_xS_y$ heterointerfaces enabling stabilization intermediates for high-performance $CO_2$ electroreduction to formate. *Nano Res.* **2023**, *16*, 7974–7981

[5] Zhao, Z. B.; Zhang, J. G.; Lei, M.; Lum, Y. Reviewing the impact of halides on electrochemical $CO_2$ reduction. *Nano Res. Energy.* **2023**, *2*, e9120044.

[6] Yang, X.; Li, Q. X.; Chi, S. Y.; Li, H. F.; Huang, Y. B.; Cao, R. Hydrophobic perfluoroalkane modified metal-organic frameworks for the enhanced electrocatalytic reduction of $CO_2$. *SmartMat* **2022**, *3*, 163–172.

[7] Yang, P. P.; Gao, M. R. Enrichment of reactants and intermediates for electrocatalytic $CO_2$ reduction. *Chem. Soc. Rev.* **2023**, *52*, 4343–4380.

[8] Duanmu, J. W.; Gao, M. R. Advances in bio-inspired electrocatalysts for clean energy future. *Nano Res.*, in press, https://doi.org/10.1007/s12274-023-5977-3.

[9] Deng, W. Y.; Zhang, P.; Seger, B.; Gong, J. L. Unraveling the rate-limiting step of two-electron transfer electrochemical reduction of carbon dioxide. *Nat. Commun.* **2022**, *13*, 803.

[10] Gu, Z. X.; Shen, H.; Chen, Z.; Yang, Y. Y.; Yang, C.; Ji, Y. L.; Wang, Y. H.; Zhu, C.; Liu, J. L.; Li, J. et al. Efficient electrocatalytic $CO_2$ reduction to $C_{2+}$ alcohols at defect-site-rich Cu surface. *Joule* **2021**, *5*, 429–440.

[11] Wang, M. L.; Yao, Y.; Tian, Y. H.; Yuan, Y. F.; Wang, L. G.; Yang, F. Y.; Ren, J. J.; Hu, X. R.; Wu, F.; Zhang, S. Q. et al. Atomically dispersed manganese on carbon substrate for aqueous and aprotic $CO_2$ electrochemical reduction. *Adv. Mater.* **2023**, *35*, 2210658.

[12] Zhu, Y. T.; Cui, X. Y.; Liu, H. L.; Guo, Z. G.; Dang, Y. F.; Fan, Z. X.; Zhang, Z. C.; Hu, W. P. Tandem catalysis in electrochemical $CO_2$ reduction reaction. *Nano Res.* **2021**, *14*, 4471–4486.

[13] Niu, Z. Z.; Chi, L. P.; Wu, Z. Z.; Yang, P. P.; Fan, M. H.; Gao, M. R. $CO_2$-assisted formation of grain boundaries for efficient CO–CO coupling on a derived Cu catalyst. *Natl. Sci. Rev.* **2023**, *2*, 20220044.

[14] Lai, W. C.; Qiao, Y.; Wang, Y. N.; Huang, H. W. Stability issues in electrochemical $CO_2$ reduction: Recent advances in fundamental understanding and design strategies. *Adv. Mater.* **2023**, *35*, 2306288.

[15] Huang, M.; Deng, B. W.; Zhao, X. L.; Zhang, Z. Y.; Li, F.; Li, K. L.; Cui, Z. H.; Kong, L. X.; Lu, J. M.; Dong, F. et al. Template-sacrificing synthesis of well-defined asymmetrically coordinated single-atom catalysts for highly efficient $CO_2$ electrocatalytic reduction. *ACS Nano* **2022**, *16*, 2110–2119.

[16] Ge, H.; Kuwahara, Y.; Kusu, K.; Bian, Z.; Yamashita H.

Ru/$H_xMoO_{3-y}$ with plasmonic effect for boosting photothermal catalytic $CO_2$ methanation. *Appl. Catal. B: Environ.* **2022**, *317*, 121734.

[17] He, J. L.; Jin, Z. H.; Gan, F. L.; Xie, L. L.; Guo, J. D.; Zhang, S. H.; Jia, C. Q.; Ma, D.; Dai, Z. D.; Jiang, X. Liquefiable biomass-derived porous carbons and their applications in $CO_2$ capture and conversion. *Green Chem.* **2022**, *24*, 3376–3415.

[18] Zhang, W.; Jia, B. H.; Liu, X.; Ma, T. Y. Surface and interface chemistry in metal-free electrocatalysts for electrochemical $CO_2$ reduction. *SmartMat* **2022**, *3*, 5–34.

[19] Sun, M. Z.; Wong, H. H.; Wu, T.; Lu, Q. Y.; Lu, L.; Chan, C. H.; Chen, B. A.; Dougherty, A. W.; Huang, B. L. Double-dependence correlations in graphdiyne-supported atomic catalysts to promote $CO_2$RR toward the Generation of $C_2$ products. *Adv. Energy Mater.* **2023**, *13*, 2203858.

[20] Jin, S.; Hao, Z. M.; Zhang, K.; Yan, Z. H.; Chen, J. Advances and challenges for the electrochemical reduction of $CO_2$ to CO: From fundamentals to industrialization. *Angew. Chem., Int. Ed.* **2021**, *60*, 20627–20648.

[21] Zhu, J. B.; Xiao, M. L.; Ren, D. Z.; Gao, R.; Liu, X. Z.; Zhang, Z.; Luo, D.; Xing, W.; Su, D.; Yu, A. et al. Quasi-covalently coupled Ni–Cu atomic pair for synergistic electroreduction of $CO_2$. *J. Am. Chem. Soc.* **2022**, *144*, 9661–9671.

[22] Zhao, Q. L.; Wang, Y. A.; Li, M.; Zhu, S. Q.; Li, T. H.; Yang, J. X.; Lin, T.; Delmo, E. P.; Wang, Y. N.; Jang, J. et al. Organic frameworks confined Cu single atoms and nanoclusters for tandem electrocatalytic $CO_2$ reduction to methane. *SmartMat* **2022**, *3*, 183–193.

[23] Li, Y. Z.; Chen, J. L.; Chen, S.; Liao, X. L.; Zhao, T. T.; Cheng, F. Y.; Wang, H. *In situ* confined growth of bismuth nanoribbons with active and robust edge sites for boosted $CO_2$ electroreduction. *ACS Energy Lett.* **2022**, *7*, 1454–1461

[24] Wang, T.; Chen, J. D.; Ren, X. Y.; Zhang, J. C.; Ding, J.; Liu, Y. H.; Lim, K. H.; Wang, J. H.; Li, X. N.; Yang, H. et al. Halogen-incorporated Sn catalysts for selective electrochemical $CO_2$ reduction to formate. *Angew. Chem., Int. Ed.* **2023**, *62*, e202211174.

[25] Xiao, T. S.; Tang, C.; Li, H. B.; Ye, T.; Ba, K.; Gong, P.; Sun, Z. Z. $CO_2$ reduction with coin catalyst. *Nano Res.* **2022**, *15*, 3859–3865

[26] Dai, S.; Huang, T. H.; Liu, W. I.; Hsu, C. W.; Lee, S. W.; Chen, T. Y.; Wang, Y. C.; Wang, J. H.; Wang, K. W. Enhanced $CO_2$ electrochemical reduction performance over Cu@AuCu catalysts at high noble metal utilization efficiency. *Nano Lett.* **2021**, *21*, 9293–9300.

[27] Li, Z.; Wu, R.; Zhao, L.; Li, P. B.; Wei, X. X.; Wang, J. J.; Chen, J. S.; Zhang, T. R. Metal-support interactions in designing noble metal-based catalysts for electrochemical $CO_2$ reduction: Recent advances and future perspectives. *Nano Res.* **2021**, *14*, 3795–3809.

[28] Vijay, S.; Ju, W.; Brückner, S.; Tsang, S. C.; Strasser, P.; Chan, K. Unified mechanistic understanding of $CO_2$ reduction to CO on transition metal and single atom catalysts. *Nat. Catal.* **2021**, *4*, 1024–1031.

[29] Guo, F. J.; Zhang, M. Y.; Yi, S. C.; Li, X. X.; Xin, R.; Yang, M.; Liu, B.; Chen, H. B.; Li, H. M.; Liu, Y. J. Metal-coordinated porous polydopamine nanospheres derived $Fe_3N$-FeCo encapsulated N-doped carbon as a highly efficient electrocatalyst for oxygen reduction reaction. *Nano Res. Energy.* **2022**, *1*, 9120027.

[30] Wu, G.; Zheng, X. S.; Cui, P. X.; Jiang, H. Y.; Wang, X. Q.; Qu, Y. T.; Chen, W. X.; Lin, Y.; Li, H.; Han, X. et al. A general synthesis approach for amorphous noble metal nanosheets. *Nat. Commun.* **2019**, *10*, 4855.

[31] Cao, B.; Li, F. Z.; Gu, J. Designing Cu-based tandem catalysts for $CO_2$ electroreduction based on mass transport of CO intermediate. *ACS Catal.* **2022**, *12*, 9735–9752.

[32] Chen, S. Y.; Li, X. Q.; Kao, C. W.; Luo, T.; Chen, K. J.; Fu, J. W.; Ma, C.; Li, H. M.; Li, M.; Chan, T. S. et al. Unveiling the proton-feeding effect in sulfur-doped Fe-N-C single-atom catalyst for enhanced $CO_2$ electroreduction. *Angew. Chem., Int. Ed.* **2022**, *61*, e202206233.

[33] Guo, Y.; Wang, Y. C.; Shen, Y.; Cai, Z. Y.; Li, Z.; Liu, J.; Chen, J. W.; Xiao, C.; Liu, H. C.; Lin, W. B. et al. Tunable cobalt-polypyridyl catalysts supported on metal-organic layers for electrochemical $CO_2$ reduction at low overpotentials. *J. Am. Chem. Soc.* **2020**, *142*, 21493–21501.

[34] Feng, J. Q.; Gao, H. S.; Zheng, L. R.; Chen, Z. P.; Zeng, S. J.; Jiang, C. Y.; Dong, H. F.; Liu, L. C.; Zhang, S. J.; Zhang, X. P. A Mn-$N_3$ single-atom catalyst embedded in graphitic carbon nitride for efficient $CO_2$ electroreduction. *Nat. Commun.* **2020**, *11*, 4341.

[35] Shang, H. S.; Wang, T.; Pei, J. J.; Jiang, Z. L.; Zhou, D. N.; Wang, Y.; Li, H. J.; Dong, J. C.; Zhuang, Z. B.; Chen, W. X. et al. Design of a single-atom Indium$^{\delta+}$-$N_4$ interface for efficient electroreduction of $CO_2$ to formate. *Angew. Chem., Int. Ed.* **2020**, *59*, 22465–22469.

[36] Jiang, Z. L.; Wang, T.; Pei, J. J.; Shang, H. S.; Zhou, D. N.; Li, H. C.; Dong, J.; Wang, Y.; Cao, R.; Zhuang, Z. B. et al. Discovery of main group single Sb-$N_4$ active sites for $CO_2$ electroreduction to formate with high efficiency. *Energy Environ. Sci.* **2020**, *13*, 2856–2863.

[37] Ren, B. H.; Wen, G. B.; Gao, R.; Luo, D.; Zhang, Z.; Qiu, W. B.; Ma, Q. Y.; Wang, X.; Cui, Y.; Ricardez-Sandoval, L. et al. Nano-crumples induced Sn–Bi bimetallic interface pattern with moderate electron bank for highly efficient $CO_2$ electroreduction. *Nat. Commun.* **2022**, *13*, 2486.

[38] Zhang, J. W.; Zeng, G. M.; Chen, L. L.; Lai, W. C.; Yuan, Y. L.; Lu, Y. F.; Ma, C.; Zhang, W. H.; Huang, H. W. Tuning the reaction path of $CO_2$ electroreduction reaction on indium single-atom catalyst: Insights into the active sites. *Nano Res.* **2022**, *15*, 4014–4022.

[39] Yuan, Y. L.; Wang, Q. Y.; Qiao, Y.; Chen, X. L.; Yang, Z. L.; Lai, W. C.; Chen, T. W.; Zhang, G. H.; Duan, H. G.; Liu, M. et al. *In situ* structural reconstruction to generate the active sites for $CO_2$ electroreduction on Bismuth ultrathin nanosheets. *Adv. Energy Mater.* **2022**, *12*, 2200970

[40] Liu, J. Y.; Li, P. S.; Bi, J. H.; Wang, Y.; Zhu, Q. G.; Sun, X. F.; Zhang, J. L.; Liu, Z. M.; Han, B. X. Sm and S co-doping to construct homo-hetero Cu catalysts for synergistic enhancing $CO_2$ electroreduction. *Chin. J. Chem.* **2023**, *41*, 1443–1449.

[41] Wei, Z. M.; Liu, Y. H.; Ding, J.; He, Q. Y.; Zhang, Q.; Zhai, Y. M. Promoting electrocatalytic $CO_2$ reduction to CO via sulfur-doped Co-N-C single-atom catalyst‡. *Chin. J. Chem.* **2023**, *41*, 3553–3559.

[42] Zhang, E. H.; Wang, T.; Yu, K.; Liu, J.; Chen, W. X.; Li, A.; Rong, H. P.; Lin, R.; Ji, S. F.; Zheng, X. S. et al. Bismuth single atoms resulting from transformation of metal-organic frameworks and their use as electrocatalysts for $CO_2$ reduction. *J. Am. Chem. Soc.* **2019**, *141*, 16569–16573.

[43] Peng, H. J.; Tang, M. T.; Liu, X. Y.; Lamoureux, P. S.; Bajdich, M.; Abild-Pedersen, F. The role of atomic carbon in directing electrochemical $CO_2$ reduction to multicarbon products. *Energy Environ. Sci.* **2021**, *14*, 473–482.

[44] Zhu, Y. Z.; Yang, X. X.; Peng, C.; Priest, C.; Mei, Y.; Wu, G. Carbon-supported single metal site catalysts for electrochemical $CO_2$ reduction to CO and beyond. *Small* **2021**, *17*, 2005148.

[45] Zhang, W. J.; Jiang, M. H.; Yang, S. Y.; Hu, Y.; Mu, B.; Tie, Z.; Jin, Z. *In-situ* grown $CuO_x$ nanowire forest on copper foam: A 3D hierarchical and freestanding electrocatalyst with enhanced carbonaceous product selectivity in $CO_2$ reduction. *Nano Res. Energy* **2022**, *1*, e9120033

[46] Boppella, R.; Austeria, P. M.; Kim, Y.; Kim, E.; Song, I.; Eom, Y.; Kumar, D. P.; Balamurugan, M.; Sim, E.; Kim, D. H. et al. Pyrrolic N-stabilized monovalent Ni single-atom electrocatalyst for efficient $CO_2$ reduction: Identifying the role of pyrrolic-N and synergistic electrocatalysis. *Adv. Funct. Mater.* **2022**, *32*, 2202351.

[47] Tang, H.; Gu, H. F.; Li, Z. Y.; Chai, J.; Qin, F. J.; Lu, C. Q.; Yu, J. Y.; Zhai, H. Z.; Zhang, L.; Li, X. Y. et al. Engineering the coordination interface of isolated Co atomic sites anchored on N-doped carbon for effective hydrogen evolution reaction. *ACS Appl. Mater. Interfaces* **2022**, *14*, 46401–46409.

[48] Hu, Y. N.; Ying, D.; Sun, Z. Y.; Li, B.; Zhou, H. X.; Wang, S.; Hu, X. M.; He, K.; Qu, M.; Chen, W. X. et al. Rational design, application and dynamic evolution of Cu-N-C single-atom catalysts. *J. Mater. Chem. A* **2022**, *10*, 21769–21796.

[49] Su, X. Z.; Jiang, Z. L.; Zhou, J.; Liu, H. J.; Zhou, D. N.; Shang, H. S.; Ni, X. M.; Peng, Z.; Yang, F.; Chen, W. X. et al. Complementary *operando* spectroscopy identification of *in-situ* generated metastable

charge-asymmetry $Cu_2$-$CuN_3$ clusters for $CO_2$ reduction to ethanol. *Nat. Commun.* **2022**, *13*, 1322.

[50] Han, G. F.; Li, F.; Rykov, A. I.; Im, Y. K.; Yu, S. Y.; Jeon, J. P.; Kim, S. J.; Zhou, W.; Ge, R.; Ao, Z. et al. Abrading bulk metal into single atoms. *Nat. Nanotechnol.* **2022**, *17*, 403–407.

[51] Yang, T.; Mao, X. N.; Zhang, Y.; Wu, X. P.; Wang, L.; Chu, M. Y.; Pao, C. W.; Yang, S. Z.; Xu, Y.; Huang, X. Q. Coordination tailoring of Cu single sites on $C_3N_4$ realizes selective $CO_2$ hydrogenation at low temperature. *Nat. Commun.* **2021**, *12*, 6022.

[52] Zhao, K.; Nie, X. W.; Wang, H. Z.; Chen, S.; Quan, X.; Yu, H. T.; Choi, W.; Zhang, G. H.; Kim, B.; Chen, J. G. Selective electroreduction of $CO_2$ to acetone by single copper atoms anchored on N-doped porous carbon. *Nat. Commun.* **2020**, *11*, 2455.

[53] Zhang, S. L.; Sun, L.; Fan, Q. N.; Zhang, F. L.; Wang, Z. J.; Zou, J. S.; Zhao, S. Y.; Mao, J. F.; Guo, Z. P. Challenges and prospects of lithium-$CO_2$ batteries. *Nano Res. Energy* **2022**, *1*, e9120001.

[54] Chen, P. Z.; Zhang, N.; Wang, S. B.; Zhou, T. P.; Tong, Y.; Ao, C. C.; Yan, W. S.; Zhang, L. D.; Chu, W. S.; Wu, C. Z. et al. Interfacial engineering of cobalt sulfide/graphene hybrids for highly efficient ammonia electrosynthesis. *Proc. Natl. Acad. Sci. USA* **2019**, *116*, 6635–6640.

[55] Tong, Y.; Chen, P. Z.; Zhou, T. P.; Xu, K.; Chu, W. S.; Wu, C.; Xie, Y. A bifunctional hybrid electrocatalyst for oxygen reduction and evolution: Cobalt oxide nanoparticles strongly coupled to B,N-decorated graphene. *Angew. Chem., Int. Ed.* **2017**, *56*, 7121–7125.

[56] Zhao, Y. S.; Yang, N. L.; Yao, H. Y.; Liu, D. B.; Song, L.; Zhu, J.; Li, S. Z.; Gu, L.; Lin, K. F.; Wang, D. Stereodefined codoping of sp-N and S atoms in few-layer graphdiyne for oxygen evolution reaction. *J. Am. Chem. Soc.* **2019**, *141*, 7240–7244.

[57] Shang, H. S.; Zhou, X. Y.; Dong, J. C.; Li, A.; Zhao, X.; Liu, Q. H.; Lin, Y.; Pei, J. J.; Li, Z.; Jiang, Z. L. et al. Engineering unsymmetrically coordinated $Cu\text{-}S_1N_3$ single atom sites with enhanced oxygen reduction activity. *Nat. Commun.* **2020**, *11*, 3049.

[58] Yang, H. H.; Chen, Y. Y.; Cui, X. J.; Wang, G. F.; Cen, Y. L.; Deng, T. S.; Yan, W. J.; Gao, J.; Zhu, S. H.; Olsbye, U. et al. A highly stable copper-based catalyst for clarifying the catalytic roles of $Cu^0$ and $Cu^+$ species in methanol dehydrogenation. *Angew. Chem., Int. Ed.* **2018**, *57*, 1836–1840.

[59] Lee, B. H.; Park, S.; Kim, M.; Sinha, A. K.; Lee, S. C.; Jung, E.; Chang, W. J.; Lee, K. S.; Kim, J. H.; Cho, S. P. et al. Reversible and cooperative photoactivation of single-atom $Cu/TiO_2$ photocatalysts. *Nat. Mater.*, **2019**, *18*, 620–626.

[60] Wu, Z. H.; Liu, Y. P.; Xing, X. Q.; Yao, L.; Chen, Z. J.; Mo, G.; Zheng, L. R.; Cai, Q.; Wang, H.; Zhong, J. J. et al. A novel SAXS/XRD/XAFS combined technique for *in-situ* time-resolved simultaneous measurements. *Nano Res.* **2023**, *16*, 1123–1131.